

Boise State University

ScholarWorks

Mechanical and Biomedical Engineering Faculty
Publications and Presentations

Department of Mechanical and Biomedical
Engineering

5-2024

Data-Driven and Cell-Specific Determination of Nuclei-Associated Actin Structure

Nina Nikitina

Boise State University

Nurbanu Bursa

Hacettepe University

Matthew Goelzer

Oral Roberts University

Madison Goldfeldt

Boise State University

Chase Crandall

Boise State University

See next page for additional authors

Publication Information

Nikitina, Nina; Bursa, Nurbanu; Goelzer, Matthew; Goldfeldt, Madison; Crandall, Chase; Howard, Sean; . . . and Uzer, Gunes. (2024). "Data-Driven and Cell-Specific Determination of Nuclei-Associated Actin Structure". *Small Structures*, 5(5), 2300204. <https://doi.org/10.1002/sstr.202300204>

Authors

Nina Nikitina, Nurbanu Bursa, Matthew Goelzer, Madison Goldfeldt, Chase Crandall, Sean Howard, Janet Rubin, Anamaria Zavala, Aykut Satici, and Gunes Uzer

Data-Driven and Cell-Specific Determination of Nuclei-Associated Actin Structure

Nina Nikitina, Nurbanu Bursa, Matthew Goelzer, Madison Goldfeldt, Chase Crandall, Sean Howard, Janet Rubin, Anamaria Zavala, Aykut Satici, and Gunes Uzer*

Quantitative volumetric assessment of filamentous actin (F-actin) fibers remains challenging due to their interconnected nature, leading researchers to utilize threshold-based or qualitative measurement methods with poor reproducibility. Herein, a novel machine learning-based methodology is introduced for accurate quantification and reconstruction of nuclei-associated F-actin. Utilizing a convolutional neural network (CNN), actin filaments and nuclei from 3D confocal microscopy images are segmented and then each fiber is reconstructed by connecting intersecting contours on cross-sectional slices. This allows measurement of the total number of actin filaments and individual actin filament length and volume in a reproducible fashion. Focusing on the role of F-actin in supporting nucleocytoplasmic connectivity, apical F-actin, basal F-actin, and nuclear architecture in mesenchymal stem cells (MSCs) are quantified following the disruption of the linker of nucleoskeleton and cytoskeleton (LINC) complexes. Disabling LINC in MSCs generates F-actin disorganization at the nuclear envelope characterized by shorter length and volume of actin fibers contributing a less elongated nuclear shape. The findings not only present a new tool for mechanobiology but introduce a novel pipeline for developing realistic computational models based on quantitative measures of F-actin.

the nucleus at the “actin cap” translate these mechanical forces into the nucleus to alter both nuclear structure and gene expression.^[1] While understanding the organization and connectivity of cytoskeletal networks has been a research topic in cell mechanobiology for many years,^[2] reconstructing the interconnected structures of branching F-actin fibers remains a technical barrier. Much of the information regarding F-actin organization relies on manual and semiautomated processing of 2D images through open-source programs such as imageJ;^[3] these methods yield qualitative information with poor quantitative numbers for molecular structures. Furthermore, 3D reconstruction of F-actin represents another challenge as these methods generally represent the cytoskeleton as a simple planar geometry^[4–6] precluding the development of models that recapture the full complexity of cellular cytoskeletal networks. To provide quantitative information from planar analysis, fluorescence and electron microscopy-based


1. Introduction

Mechanical information is translated into biological response through perturbations of a highly organized and connected filamentous actin (F-actin) cytoskeleton where linker of nucleoskeleton and cytoskeleton (LINC)-mediated F-actin connections to

image analysis methods have been developed to analyze biopolymer properties, including number, length, and organization. Reconstruction methods typically involve enhancing filamentous features to identify and isolate filaments in images, separating filaments from the background, and extracting individual filaments using line segment detectors.^[7–10] Aside from these

N. Nikitina, M. Goldfeldt, C. Crandall, S. Howard, A. Zavala, A. Satici, G. Uzer
Boise State University
Department of Mechanical & Biomedical Engineering
1910 University Drive, Boise 83725, USA
E-mail: gunesuzer@boisestate.edu

N. Bursa
Institute for Modeling Collaboration and Innovation
University of Idaho
Moscow 83844, USA

 The ORCID identification number(s) for the author(s) of this article can be found under <https://doi.org/10.1002/ssstr.202300204>.

© 2024 The Authors. Small Structures published by Wiley-VCH GmbH. This is an open access article under the terms of the Creative Commons Attribution License, which permits use, distribution and reproduction in any medium, provided the original work is properly cited.

DOI: 10.1002/ssstr.202300204

N. Bursa
Department of Statistics
Hacettepe University
Ankara 06800, Turkey

M. Goelzer
Department of Biomedical Engineering
Oral Roberts University
Tulsa 74171, USA

J. Rubin
Department of Medicine
University of North Carolina at Chapel Hill
Chapel Hill 27599, USA

planar approaches, only few studies have been conducted on the process of separating cytoskeletal filaments and networks in 3D using immunofluorescence microscopy images.^[11,12] While such methods have provided valuable information, reproducible volumetric quantification of F-actin is still beyond the reach of many research groups necessitating an easy-to-use, unbiased and repeatable volumetric reconstruction of dynamic cytoskeletal networks in cells.

LINC complexes formed by a family of proteins that include KASH (Klarsicht, ANC-1, Syne Homology) and SUN (Sad1p, UNC-84) domains provide mechanical connection between cytoplasmic and nuclear compartments. LINC-mediated nucleocytoplasmic connectivity has been shown to play important roles in mechanosensitivity,^[13,14] chromatin organization,^[15–17] and DNA repair mechanisms.^[18,19] Here, utilizing intact and LINC-disabled mesenchymal stem cells (MSCs), we describe a novel approach for automating reconstruction of the nucleocytoplasmic architecture that is based on deep learning-assisted image analysis and segmentation of cross-sectional image slices. Focused on the actin fiber architecture within the nuclear region, our method provides precise reconstruction of nuclei-associated fibers, nuclei, and enables extraction of associated statistical data. The software package developed for this method, “afilement”, is publicly available for use and validation (see Data Availability section). Using the afilement software and confocal images of primary MSCs, we have further quantitatively compared the cell-specific consequences of disabling LINC complex on the F-actin cytoskeleton.

2. Methods and Data Collection

2.1. Cell Culture

Bone marrow-derived MSCs (mdMSCs) from 8 to 10 week male C57BL/6 mice were isolated as described from multiple mouse donors and MSCs pooled, providing a heterogenous MSCs cell line.^[20] Briefly, tibial and femoral marrow were collected in RPMI-1640, 9% fetal bovine serum (FBS), 9% horse serum (HS), 100 µg/ml pen/strep, and 12 µM L-glutamine. After 24 h, nonadherent cells were removed by washing with phosphate-buffered saline (PBS) and adherent cells were cultured for 4 weeks. Passage 1 cells were collected after incubation with 0.25% trypsin/1 mM EDTA × 2 min and replated in a single 175 cm² flask. After 1–2 weeks, passage 2 cells were replated at 50 cells/cm² in expansion medium (Iscove's Modified Dulbecco's Medium [IMDM], 9% FBS, 9% HS, antibiotics, L-glutamine). mdMSCs were replated every 1–2 weeks for two consecutive passages up to passage 5 and tested for osteogenic and adipogenic potential, and subsequently frozen.

These isolated MSC stocks were stably transduced with a doxycycline-inducible plasmid expressing an mCherry-tagged dominant-negative KASH (dnKASH) domain.^[21] The dnKASH plasmid was lentiviral packaged as a generous gift from Dr. Daniel Conway (Addgene # 125 554). In order to label actin in living MSCs, RFP-tagged chromobody against actin was used (Chromotek acr-TagRFP). Prior to usage, chromobody was packaged into a lentivirus for stable transfection. For both doxycycline-inducible dnKASH and chromobody, lentivirus

supernatant was added to growth media with polybrene (5 µg/ml). Lentivirus growth media mixture was added to 50%–70% confluent MSCs. Lentivirus media was replaced 48 h later with selection media containing G418 (1 mg ml^{−1}) for 5 d to select stably infected dnKASH-MSCs or chromobody expressing MSCs. Calf serum was obtained from Atlanta Biologicals (Atlanta, GA). MSCs were maintained in IMDM with FBS (10%, v/v) and penicillin/streptomycin (100 µg/ml). For immunostaining experiments, seeding cell density was 3,000 cells per cm² in growth media. Twenty-four hours after seeding, dnKASH cells were given growth media containing doxycycline (1 µg/ml).

2.2. RNA-seq

Total RNA was extracted using RNeasy (Qiagen) for three samples per group. Total RNA samples were sent to Novogene for mRNA sequencing and analysis. Briefly, the index of the reference genome was built using Hisat2 v2.0.5 and paired-end clean 2 reads were aligned to the reference genome using Hisat2 v2.0.5. featureCounts v1.5.0-p3 was used to count the reads numbers mapped to each gene. Differential expression analysis was performed using the DESeq2 R package (1.20.0). DESeq2 provides statistical routines for determining differential expressions in digital gene expression data using a model based on the negative binomial distribution. The resulting *p*-values were adjusted using the Benjamini and Hochberg's approach for controlling the false discovery rate. Genes with an adjusted *p*-value < 0.05 and fold change > 0.2 found by DESeq2 were assigned as differentially expressed. Genes with significant differential gene expression were further analyzed with DAVID for pathway analysis.^[22] Pathways with a *p* < 0.05 were selected.

2.3. Immunofluorescence

Forty-eight hours after dnKASH expression, cells were fixed with 4% paraformaldehyde. Cells were permeabilized by incubation with 0.1% Triton X-100. Cells were incubated in a blocking serum consisting of PBS with 1% bovine serum albumin. Reagents used for immunofluorescence and their concentrations are listed in Supplementary Table S1, Supporting Information. For nuclear staining, cells were incubated with NucBlue Hoechst 33 342 stain (Fisher Scientific) according to the manufacturer's protocol. F-actin was stained using Phalloidin (0.1 µM, iFluor 488, Cayman Chemicals). The fluorescent actin cytoskeleton images were obtained using a Leica Stellaris 5 confocal system configured with a Leica DMi8 inverted microscope and 63x/1.4 Oil HC PL APO objective. Live cell imaging was performed in Zeiss LSM 900 confocal microscope with an environmental chamber using 40x oil immersion objective.

2.4. Reconstruction of Apical and Basal Actin Stress Fibers of MSC from Confocal Microscope Images

The reconstruction algorithm is divided into three phases: confocal image preprocessing, deep learning image segmentation, and postprocessing (Figure 1).

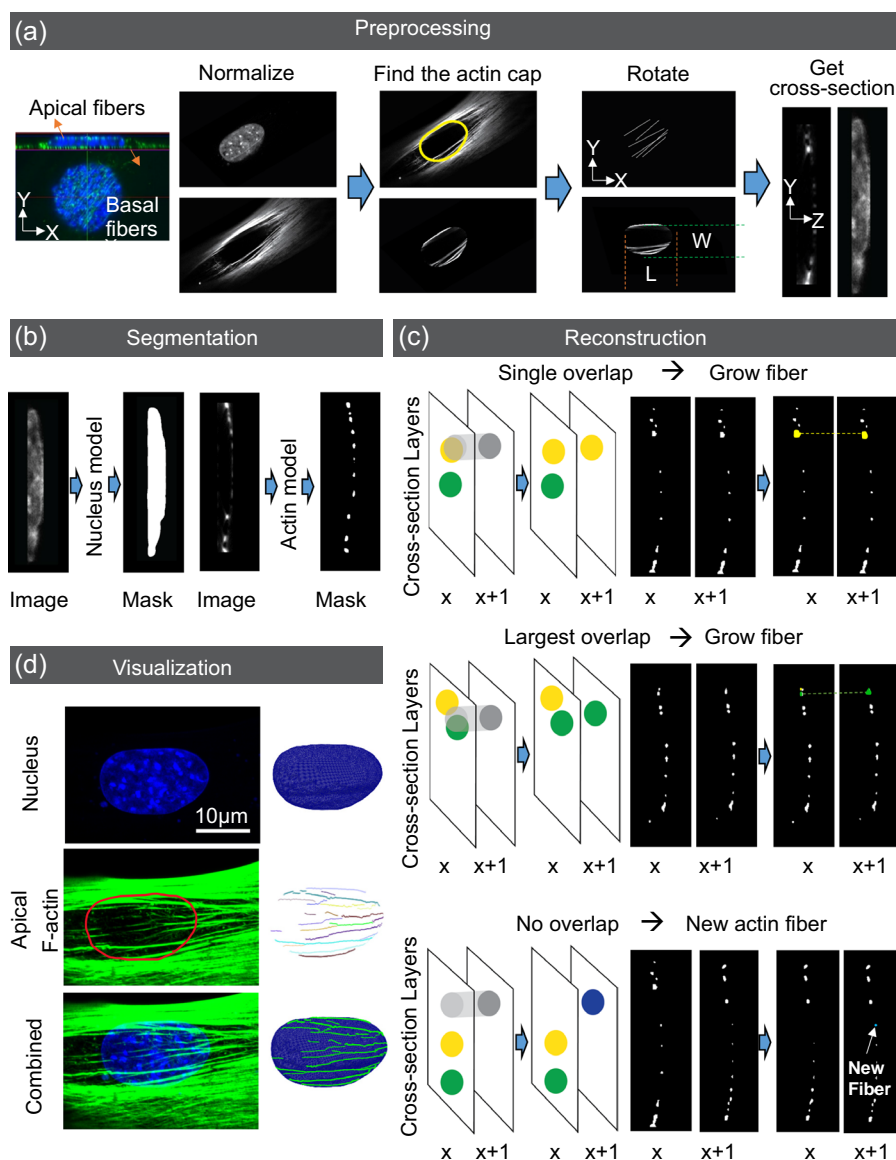


Figure 1. Stress fiber reconstruction algorithm. a) Image preprocessing algorithm reads images and metadata, normalizes the images, cuts out the region corresponding to the nucleus location, rotates the image to align fibers based on Hough Transformation (Methods) of maximal projection of a fiber layer, and converts the processed single-cell image layers into cross-sectional layers. b) Segmentation process for actin fibers and nuclei in Y–Z cross-sectional confocal images using two distinctly trained U-Net CNN models. c) Actin fiber reconstruction process based on contour intersections across successive cross-sectional layers of actin masks. In this process, contours of detected F-actin blobs on cross-sectional masks are extended from the initial layer. These contours are methodically connected to corresponding ones on subsequent layers, following specific overlap criteria: 1) Straightforward continuation: A single contour from layer $x + 1$ overlaps exclusively with one contour from layer x . This indicates a direct continuation of the actin fiber. 2) Overlap with multiple contours: When a contour from layer $x + 1$ overlaps with several contours from the previous layer x , it is integrated into the fiber with the contour that has the largest overlap area. This scenario often represents a branching point. 3) Formation of a new actin fiber: If a contour on layer x does not overlap with any contours from the preceding layer $x + 1$, a new actin fiber object is formed, signifying the start of a separate fiber. d) A side-by-side comparison of original confocal microscopy images and their respective 3D reconstructions. MSCs were fixed with 4% paraformaldehyde and stained against F-actin (Phalloidin) and nucleus (Hoechst). Filament reconstruction of nucleus is shown in blue and actin is shown in green. The top panel shows the nucleus and its mesh reconstruction. The middle panel displays the actin fibers superimposed on the nucleus. The bottom panel focuses on actin fibers, differentiated by color in the reconstruction to depict individual fiber paths.

2.4.1. Preprocessing

The preprocessing phase (Figure 1a) prepares images for segmentation. The algorithm acquires image resolution, z-stack size, and bit depth via the python-bioformats package.^[23] To detect nuclear area, thresholding was applied to each layer of the confocal image z-stack to isolate the largest circumference, which was then cropped for further analysis. To align F-actin fibers along the nucleus, fiber layers were converted into 2D via maximal projection and gross fiber orientation was detected via Hough Transform and aligned along the X-axis. This rotation allows detection of fibers through Y–Z cross-sectional view along the X-axis. As apical and basal fibers are not necessarily parallel to each other,^[24] we preprocessed basal and apical fibers separately. To optimize reconstruction efficiency for apical fiber analysis, rotation was based on maximal projection of the top 50% of the height and the bottom 50% was designated as the basal fibers. Finally, these rotated sets of nuclei and F-actin images were converted into Y–Z cross-sectional layer sets along the X-axis.

2.4.2. Image Segmentation

Actin fibers on Y–Z cross-sectional images appear as discrete dots which vary in size, shape, and intensity across stacked layers along the X-axis. Because of this heterogeneity, applying a global detection threshold was not possible and required user-directed manual thresholding for each layer. To both reduce the input parameters from the user and provide unbiased detection, cross-sectional images of the actin and nucleus channels were segmented utilizing a trained convolutional neural network based on a U-Net architecture (Figure 1b).^[25,26]

The use of the U-Net architecture is compelling because of its good performance (precise segmentation) even in the absence of thousands of training images. Indeed, it is difficult to obtain a myriad of training images because a human operator must tend to each image and provide segmentation of the actin fibers and nuclei, which becomes overwhelming after a few hundred images are processed. The U-Net convolutional neural network architecture comprises an encoder–decoder (contracting–expansive) structure, where the encoder and the decoder are almost symmetric and yield a U-shaped architecture. This architecture makes excessive use of data augmentation by applying elastic deformations to the available training images.

Training and validation image sets were generated manually by labeling each F-actin dot and nuclei border on Y–Z cross-sectional images. For the training and validation sets, we randomly selected 44 cross-sectional slices for actin and 41 slices for the nucleus, drawing from images of two distinct cells. The sliced images were padded to a size of 512 × 512 pixels, and a total number of 44 images were split into 38 for training and 6 for validation for actin and 41 images were split into 35 for training and 6 for validation for nucleus. Parameters for learning were: learning rate—0.001, batch size—1, and number of epochs—200. We used a graphics processing unit to speed up the training process. The neural network minimizes the loss function during training that quantifies the pixel-to-pixel differences between the predicted and target image (Figure 2b). We changed the loss function to increase the error for false-negative results

for actin fibers to 200 and nucleus to 20. Apical and basal fibers were assigned based on the mean Z coordinate of each fiber point; if the mean is higher than the nucleus center, then the fiber is labeled as apical, and if it is lower than the nucleus center, then the fiber is tagged as a basal fiber.

2.4.3. Reconstruction

As depicted in Figure 1b, to reconstruct individual F-actin structures, we grew each of the detected F-actin dots (will be referred as contours) from the first layer by connecting them to the detected contours on the next layer if it satisfied the overlap criterion from the previous layer mask. If the contour did not overlap with any other contour from the previous layer, a new actin fiber object was created. If the contour overlapped with more than one contour from the previous layer (i.e., branching points), the contour was added to a fiber whose contour had the biggest overlap area. For example, if two contours on the current layer overlapped the same contour on the previous layer, the contour with the larger overlapping area was added to the existing actin fiber object, and a new actin fiber object created for the second contour. At the end of the reconstruction, all fibers smaller than 1 μm in length were filtered out (optional parameter). Fiber length and volume were measured for each specific fiber within each cell in the dataset. Aggregated fiber statistics on a cellular level include the total fiber volume, length, and count of apical fibers, basal fibers, and the whole cell (apical + basal).

To reconstruct the nucleus, the contours of the nucleus shape on each Y–Z plane were combined together as a nucleus object. Volume was measured for the reconstructed object. Length was measured as the length of the rotated nucleus projection on the X-axis, width on the Y-axis, and the height extracted by applying the ellipsoid volume formula: $(4/3) \times \pi \times R1 \times R2 \times R$.

Figure 1d demonstrates a side-by-side comparison of raw confocal images with algorithmic reconstruction results. A more detailed validation of the algorithm's accuracy is presented in Results section.

2.5. Statistical Analysis

The statistical analyses in Figure 4 and 5, S3, and S4, Supporting Information, as well as Table 1 and 2 were based on a dataset containing 19 nontreated (–Dox) and 26 treated (+Dox) cells with 12 variables (basal fiber length, apical fiber length, total fiber length, basal fiber volume, apical fiber volume, total fiber volume, basal fiber number, apical fiber number, total fiber number, nucleus width, nucleus length, and nucleus volume). To reduce the confounding bias and to obtain treated and nontreated cells with similar characteristics, propensity score matching was used with the nearest neighbor method. When calculating the propensity score, a 1:1 allocation ratio based on the nucleus volume variable was used. Thus, 19 treated cells were selected from 26 treated cells that were most statistically similar to the 19 cells in the nontreated group.

All statistical analyses were applied using R-software, version 4.1.3 (R Core Team, 2022) and the RStudio graphical interface. Shapiro–Wilk test was used to determine whether the variables were distributed normally. Continuous variables are presented as

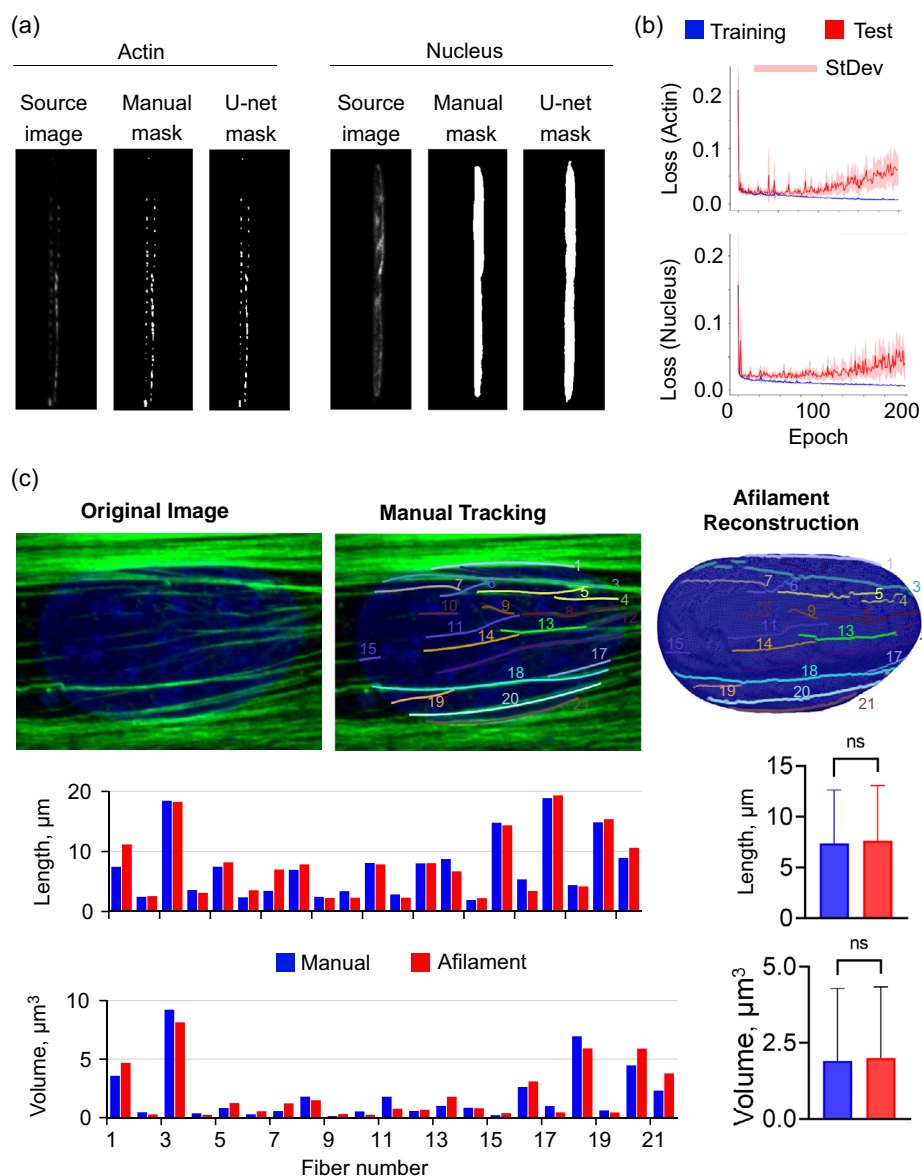


Figure 2. Afilament algorithm successfully labels nuclei-associated actin fibers. a) Comparative segmentation analysis: side-by-side views of the cross-sectional slice from the original confocal microscopy images alongside the manual and U-Net-derived segmentation masks for both actin and nucleus. This visual comparison shows the actin and nucleus model's segmentation capabilities, with the U-Net masks closely mirroring the precision of manual annotations. b) Training details for the neural network. The learning parameters used were a learning rate of 0.001, a batch size of 1, and 200 epochs. The loss function, which quantifies the differences between predicted and target images, was minimized during training. To prioritize false-negative results the loss function was adjusted to increase the error by 200 for actin fibers and by 20 for nucleus model. c) Comparative analysis between manual measurements and algorithmic estimations of actin fibers' lengths and volumes. MSCs were fixed with 4% paraformaldehyde and stained against F-actin (Phalloidin) and nucleus (Hoechst). The manual measurements were obtained using ImageJ tools, while the algorithmic data were derived from an afilement algorithm. A paired t -test was conducted to evaluate the differences between the two sets of measurements for both actin fiber length and volume. The average length of apical actin fibers measured manually is 7.36 μm , compared to 7.64 μm for the afilement algorithm ($p = 0.3760$). Similarly, for fiber volume, the manual measurement is 1.91 μm^3 , and the algorithmic estimation is 2.01 μm^3 , also yielding a nonsignificant difference ($p = 0.5109$).

mean \pm standard deviation or median (quartile deviation) according to their normality (Table 1). The Spearman correlation coefficient was used to examine correlations between variables (Figure 5c). When comparing the variables between groups, bootstrap t -test with 1000 replications was preferred because of the

small sample size. Two-tailed p -value ≤ 0.05 was considered statistically significant in analyses. In addition to p -values, r effect sizes were also calculated for comparisons.

To see the effects and odds ratios of variables, both a univariate logistic regression model and a multiple logistic regression

Table 1. Characteristics of dataset. Bold indicates p -value <0.05 ; deviations of continuous variable were presented either as mean \pm standard deviation or as median (quartile deviation) according to their normality.

Variables	Nontreated	Treated	p -value	Effect size
Nucleus volume	1620.53 (628.26)	1187.58 \pm 405.51	0.138	–
Nucleus length	30.10 \pm 5.49	25.70 (2.77)	<0.001	0.560
Nucleus width	21.00 \pm 4.25	19.33 \pm 4.38	0.200	–
Total fiber number	89.84 \pm 48.12	70.16 \pm 29.73	0.158	–
Apical fiber number	64.32 \pm 32.52	49.32 \pm 41.29	0.112	–
Basal fiber number	27.00 (16.50)	23.63 \pm 14.61	0.672	–
Total fiber volume	57.66 \pm 44.78	25.21 (15.02)	0.016	0.268
Apical fiber volume	45.66 \pm 35.18	23.33 \pm 14.61	0.022	0.295
Basal fiber volume	7.84 (8.54)	6.68 (7.65)	0.463	–
Total fiber length	400.40 \pm 239.90	259.06 \pm 153.19	0.040	0.292
Apical fiber length	293.18 \pm 161.63	186.63 \pm 96.07	0.022	0.324
Basal fiber length	100.46 (64.53)	92.52 (73.82)	0.578	–

model with stepwise variable selection were used (Table 2). Redundant physical parameter measurements of each cell were reduced and described with fewer cell properties via a principal component analysis (PCA). Usage of PCA-transformed data serves to prevent multicollinearity, reduces the dimension of the dataset, and improves the classification performance. The number of principal components was determined via elbow criteria in the scree plot of eigenvalues (Figure 5b). Finally, to classify the data points as nontreated and treated groups based on selected two principal components, three different discriminant analyses were applied: linear discriminant analysis (LDA), nonlinear quadratic discriminant analysis (QDA), and mixture discriminant analysis (MDA). Accuracy rate, sensitivity, and specificity measures of confusion matrices were used for the performance evaluation of classification methods. In the below measurement criteria, true positive means the number of correct predictions for treated cells, false positive means the number of incorrect predictions for treated cells, true negative means the number of correct predictions for nontreated cells, and false negative means the number of incorrect predictions for control cells.

$$\text{Accuracy rate} = \frac{\text{True positive} + \text{True negative}}{\text{True positive} + \text{True negative} + \text{False positive} + \text{False negative}} \quad (1)$$

Table 2. Univariate and multiple binary logistic regression results. Bold indicates p -value <0.05 .

Variables	β Estimates with SE	OR [95% CI] for univariate model	p -value	β Estimates with SE	OR [95% CI] for multiple model	p -value
Nucleus length	0.277 \pm 0.010	1.319 [1.085; 1.605]	0.006	0.277 \pm 0.010	1.319 [1.085; 1.605]	0.006
Total fiber volume	0.024 \pm 0.011	1.024 [1.002; 1.047]	0.036	–	–	–
Apical fiber volume	0.033 \pm 0.015	1.034 [1.003; 1.066]	0.030	–	–	–
Total fiber length	0.004 \pm 0.002	1.004 [1.000; 1.007]	0.046	–	–	–
Apical fiber length	0.006 \pm 0.003	1.006 [1.001; 1.011]	0.027	–	–	–

$$\text{Sensitivity} = \frac{\text{True positive}}{\text{True positive} + \text{False negative}} \quad (2)$$

$$\text{Specificity} = \frac{\text{True negative}}{\text{True negative} + \text{False positive}} \quad (3)$$

A flowchart containing the scheme for all statistical analyses is demonstrated in Figure S2, Supporting Information. Raincloud plots to visualize the summary statistics of the nucleus and fibers are added in Figure S3 and S4, Supporting Information.

3. Results

3.1. Afilament Algorithm Successfully Labels Nuclei-Associated Actin Fibers

To test the segmentation performance, we used a total of 44 actin and 41 nucleus cross-sectional images, which were split: 38 training and 6 validation for actin and 35 training and 6 validation for nucleus. We first used the training set and monitored the training progression of U-net models for nucleus and actin fibers using binary cross-entropy loss function (Figure 2b). Cross-entropy loss function ($\text{Loss} = -\sum_i (y_i \times \log(p_i) + (1 - y_i) \times \log(1 - p_i))$) penalizes deviations of the algorithm's predictions from user-defined predictions with a goal of minimizing the loss during U-net training. As shown in Figure 2b, loss function exhibited a downward trend for both actin and nucleus, reaching on average to values of 0.0085 and 0.0065 at epoch 200 (blue line). In order to test the performance, we also computed the loss function for a given random test data (red line). Results show that for $n = 3$ random test datasets, the loss function value remains below 0.06 and 0.04 for actin and nucleus, respectively.

To further evaluate the accuracy, we performed a comparison of user labeling and U-net labeling of actin fibers. We analyzed a z-stack of an apical fibers on a cell manually via imageJ by tracking each fiber using a maximal projection and sampling three fiber cross sections. These measures were compared to the output from our program. As shown in Figure 2c, visually comparing a fully labeled cross sections showed alignment between the two methods. Average total actin length difference for 21 fibers between manual (7.36 μm) and algorithm (7.64 μm) calculations was -3.81% . Similarly, average actin volume showed a -5.59% difference between the manual (1.91 μm^3) and algorithm (2.01 μm^3) calculations. Fully reconstructed apical F-actin images for fixed MSCs are provided in Figure S5, Supporting Information. We have also confirmed the ability of a filament to detect fibers in fixed C2C12 muscle precursor cells

(Figure S6, Supporting Information) and live MSCs labeled against actin (Figure S7, Supporting Information).

3.2. Overexpressing Nesprin KASH Domain Disables LINC Function in MSCs

To disable LINC function, we stably infected MSCs via lentivirus harboring a doxycycline (Dox) inducible mCherry-tagged KASH domain (dnKASH-MSCs). 1 $\mu\text{g}/\text{mL}$ Dox was added to cell culture medium to induce mCherry-KASH and prevent actin linking to Nesprins on the nuclear envelope (Figure 3a, referred as +Dox). Controls were not exposed to Dox. As shown in Figure 3b, +Dox treatment increased mCherry intensity by 73% ($n = 515$, $p < 0.0001$) and decreased Nesprin-2 intensity by 63% ($n = 530$, $p < 0.0001$), measured over the nuclear area, indicating that Nesprin-2 was displaced from nucleus in mCherry expressing cells.

3.3. Disabling LINC Function Reduces Unbiased Measures of Apical but Not Basal F-actin

As shown in Figure 4a, +Dox treatment resulted in less F-actin fibers across the apical nuclear surface and changed both the

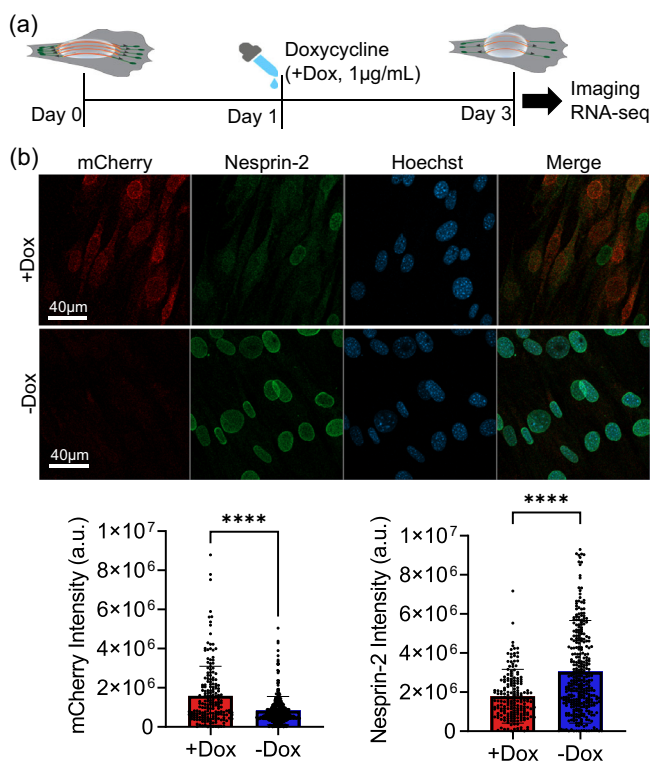


Figure 3. Overexpressing Nesprin KASH domain disables LINC function in MSCs. a) KASH expression was induced in MSCs harboring a doxycycline (Dox) inducible mCherry-tagged KASH domain by adding 1 $\mu\text{g}/\text{mL}$ Dox to cell culture medium. No Dox treatment was used as control. Imaging and RNAseq outcomes were acquired 48 h after the Dox treatment at day 3 after cell seeding. b) +Dox treatment resulted increased mCherry (red) intensity by 73% ($n = 515$, $p < 0.0001$) and decreased Nesprin-2 (green) intensity by 63% ($n = 530$, $p < 0.0001$). Nucleus was counterstained via Hoechst.

nucleus and F-actin measures. Statistical comparison of all 12 variables between Dox treated and controls are given in Table 1 and Figure S3 & S4, Supporting Information. Total fiber volume and apical fiber volume were 67% ($p = 0.016$) and 47% ($p = 0.022$) smaller in the +Dox groups, respectively. Similarly, total and actin apical fiber lengths were both 37% shorter ($p < 0.05$). As shown in Figure 4b,c, when fibers from all cells were pooled, +Dox treatment resulted in shortened total and apical fiber lengths (15%, $p < 0.001$). Total fiber volume and apical fiber volume were 30% ($p < 0.001$) and 32% ($p < 0.001$) smaller in the +Dox groups, respectively. As depicted in Figure 4c, length and volume distributions showed that control cells with no Dox treatment exhibited longer F-actin fibers with more volume: the longest fibers with the greatest volume in the -Dox group were 30%–50% larger than those in the +Dox group. Basal F-actin fiber measurements did not change. Average nucleus length was also 23% smaller in the +Dox group (Table 1, $p = 0.0007$). Taken together, these results show a significant decrease in the volume and length of actin fibers associated with the apical nuclear surface by +Dox-induced disruption of actin/Nesprin binding, resulting in a less elongated nucleus.

3.4. Disabling LINC Function Uncouples F-actin from Nuclear Shape Measures

We next explored correlations between the 12 variables across the groups. Correlation between total fiber measures, number, length, and volume, remained relatively unchanged between -Dox (0.87 ± 0.04) and +Dox (0.94 ± 0.03) groups. Fiber length, volume, and number all had lower correlations with the nucleus shape measures in the +Dox group when compared to the -Dox group (Figure 5a). For example, the average correlation of apical F-actin number, volume, and length with nuclear width, length, and volume was 0.73 ± 0.04 in the -Dox group, dropping by 50% to 0.36 ± 0.05 in the +Dox group. This indicated a strong decoupling between F-actin configuration and nuclear shape when LINC was disrupted due to the +Dox treatment.

Further univariate and multiple binary logistic regressions were applied to the dataset to find how significant variables increased the likelihood of being in one of the groups. According to Table 2, using the stepwise variable selection criteria, only the nucleus length variable was selected. As shown in Table 2, when nucleus length increases by 1 unit, the probability of being in the -Dox group increases 1.32 times compared to the +Dox, suggesting nuclear length as the most predictive measure. Next, we performed a PCA. As shown in Figure 5b, two uncorrelated principal components were found: one representing nucleus length and the other representing apical fiber length, total fiber length, apical fiber volume, and total fiber volume which explained the 95.60% of the total variance in the dataset. To test the accuracy of these two principal components, we performed discriminant analysis. To classify the cells into either treated or nontreated groups, quadratic and mixture discriminant analysis approaches were used. Results shown in Figure 5c indicate that LDA and QDA performed similarly, while MDA showed the best classification accuracy rate (87%), sensitivity (84%), and specificity (90%). Together these findings

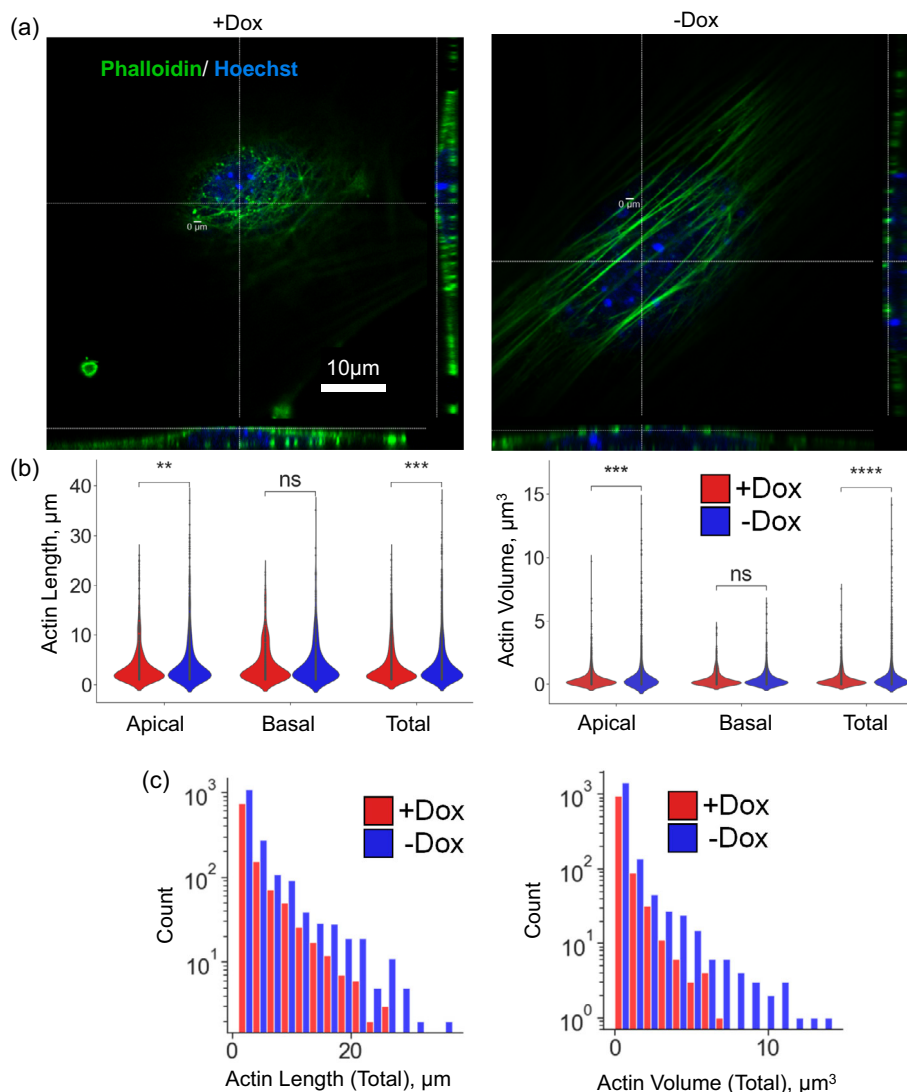


Figure 4. Disabling LINC function reduces unbiased measures of apical but not basal F-actin. a) MSCs were fixed with 4% paraformaldehyde and stained against F-actin (Phalloidin) and nucleus (Hoechst). Visualization of +Dox treatment indicates less and disorganized F-actin fibers across the apical nuclear surface. b) When fibers from all cells were combined, +Dox treatment resulted in shortened total and apical fiber lengths (15%, $p < 0.001$). Total fiber volume and apical fiber volume were 30% ($p < 0.001$) and 32% ($p < 0.001$) smaller in the +Dox groups, respectively. No changes in basal actin were observed. c) Similarly, combined distribution of total actin length and volume showed that –Dox treatment exhibited longer actin fibers with larger volumes.

support that our unbiased approach can predict whether LINC function is disabled by querying nuclear length.

3.5. LINC Depletion Alters Cell Attachment and Actin-Related Gene Expression in MSCs

Finally, to understand the possible transcriptional changes due to alterations in the actin and nucleus under +Dox treatment, we performed RNA-seq analysis. DESEQ2 analyzes filtered gene pairs with significant expression differentials ($p < 0.05$). As shown in **Figure 6a**, a hierarchical heatmap showed a clustering of +Dox treatments (i.e., dnKASH expression). As shown in **Figure 6b**, a total of 177 genes (127 up, 50 down) were

differentially regulated between +Dox and –Dox groups with $p < 0.05$ statistical significance. Comparing the gene profiles between the ±Dox groups, DAVID analyses identified 38 differentially expressed pathways. Downregulated genes only associated with two pathways (total of five genes). Upregulated pathways included cell migration, integrin binding, integrin signaling, and cell adhesion-related pathways. As shown in **Figure 6c**, quantification of cytoskeleton and cell adhesion-related genes revealed that +Dox treatment significantly increased the expression of 17 genes including adhesion G protein-coupled receptor G1 (Agdrg1)^[27] and CD93^[28] which have roles in RhoA-mediated cell spreading and migration, as well as integrin subunit beta 3 (itgb3), integrin subunit beta 7 (itgb7), and tyrosine-protein kinase Src (Src). The DAVID

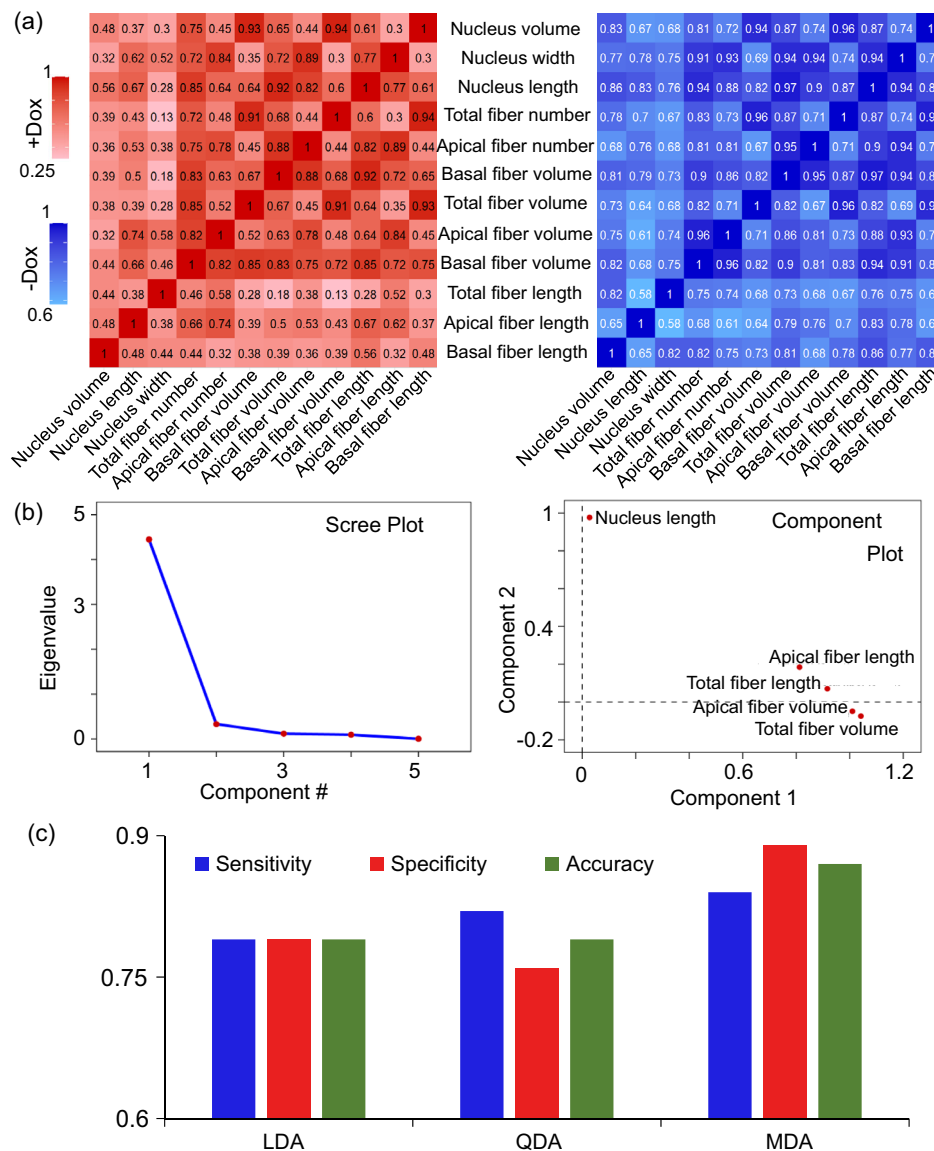


Figure 5. Disabling LINC function uncouples F-actin from nuclear shape measures. a) Correlations of +Dox and -Dox groups, from left to right. Correlation between total fiber measures remained relatively unchanged between the +Dox (0.87 ± 0.04) and the -Dox (0.94 ± 0.03) groups. Average correlation of apical F-actin measures with nuclear width, length, and volume (0.73 ± 0.04) seen a 50% drop in the +Dox group and reduced to 0.36 ± 0.05 . b) Scree plot of the eigenvalues (left) and rotated principal components plot (right). Two uncorrelated principal components were found, one representing nucleus length and the other representing apical fiber length, total fiber length, apical fiber volume, and total fiber volume which explained the 95.60% of the total variance in the dataset. c) Linear, quadratic, and mixture discriminant analysis approaches were used to classify the cells into either treated or nontreated groups. LDA and QDA performed similarly, while MDA showed the best classification accuracy rate (87%), sensitivity (84%), and specificity (90%).

pathway analyses can be found in Table S2 and S3, Supporting Information. The increased levels of integrin and cell spreading-related genes in +Dox-treated cells indicate a compensatory mechanism by which cells might respond to loss of apical actin filament volume by upregulating RhoA-mediated cell spreading.

4. Conclusions and Discussion

Here, we developed an automated volumetric detection method for cell nuclei and nuclei-associated F-actin fibers. Our method

requires no user input for segmentation and allows unbiased analysis of confocal images. This approach enables an unbiased analysis of confocal images, substantially improving processing time. The manual method of analyzing cells for verification algorithm accuracy (Figure 2c) took an estimated 4 h, whereas the automated algorithm accomplished the task in just 20 min. Although these durations may vary depending on computational power and individual proficiency, the algorithm's primary benefit is its ability to provide uniform measurement standards. Versatile postprocessing options based on user needs can be

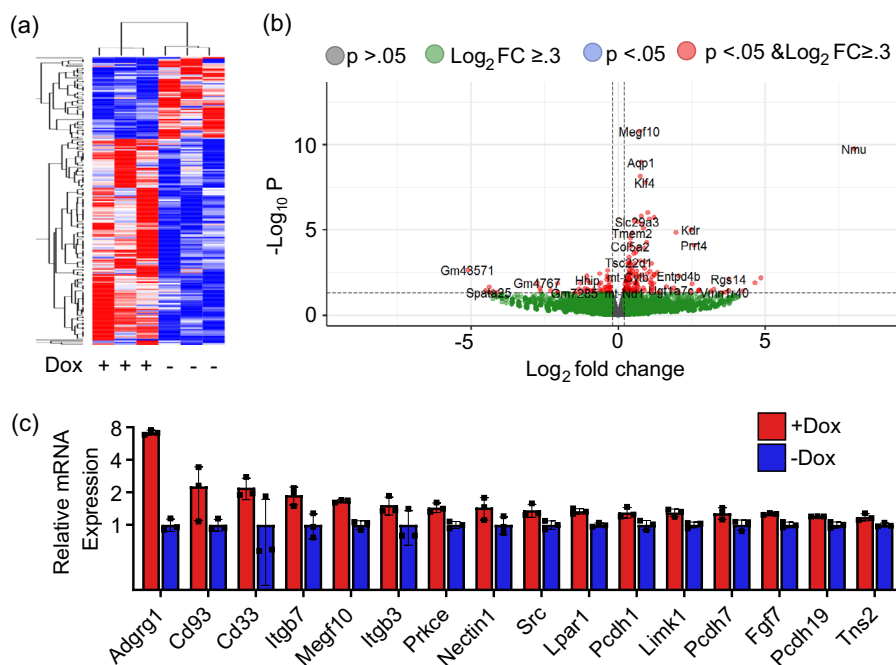


Figure 6. LINC Depletion alters cell attachment and actin-related gene expression in MSCs. a) DESEQ2 analyzes filtered gene pairs with significant expression differentials ($p < 0.05$). Hierarchical heatmap showed a clustering of +Dox treatments. b) Total of 177 genes (127 up, 50 down) were differentially regulated between +Dox and -Dox groups with $p < 0.05$ statistical significance. c) Quantification of cytoskeleton and cell adhesion-related genes revealed significantly increased expression in +Dox-treated groups.

adapted to allow detection of large range of F-actin structures associated with nuclei. As shown by quantification of a relatively small dataset, this approach permits a comprehensive statistical analysis of F-actin structure and should lend itself to high-throughput approaches when coupled with automated data collection, available through most of the modern microscopes. As most in vitro investigations also rely on sampling relatively small number of cells in an imaging plate, such unbiased, high throughput capabilities that detect inherent variations in single dish will expand cytoskeletal analysis options and aid repeatability of data across multiple laboratories. We show that our method can be implemented with multiple fixed cell types (Figure S5 & S6, Supporting Information) and live cell imaging (Figure S7, Supporting Information). In our investigations, however, we were not able to detect apical or basal fiber in muscle tissue (data not shown), suggesting that in vivo detection of nuclei-associated fibers may be more technically challenging due to increased imaging complexity.

Analyzing F-actin and nuclear shape parameters in LINC-disabled MSCs showed that depleting LINC function does not decrease the total number of fibers on the apical nuclear surface but instead shortens their overall length and volume. Interestingly we did not detect any changes in the number or characteristics of basal F-actin fibers, perhaps indicating that Nesprin is not involved. On the apical aspect, F-actin-generated contractile forces indent the nuclear surface^[29–31] magnitude of which are likely proportional to the cross section of the F-actin fibers. Our method predicts that force across the apex of the nucleus should be reduced by disrupting LINC because F-actin

volume decreased but their numbers stayed the same, likely due to a reduction in the cross section of each fiber. Such an unbiased method to detect and quantify F-actin should contribute to understand cytoskeletal forces on the nucleus. For example, mechanical models of cells often rely on simple and idealized geometries to represent cells and cytoskeleton.^[32–35] Unbiased segmentation of F-actin and nuclei from confocal scans will allow more complex and realistic cellular models and thus enable researchers to quantify nuclear forces more accurately.

Using statistical models our data was able to distinguish -Dox-treated cells from +Dox-treated cells based on the nuclear length. This was possible because disabling LINC function reduced the correlation between F-actin and nuclear shape measures by half, indicating that F-actin regulation and nuclear shape were uncoupled in LINC-disabled MSCs. Our results further indicated that the LINC-disabled state was accompanied by upregulation of genes involved in cell attachment, integrin signaling, and actin regulatory pathways. Similar increases in focal adhesion structure have been reported when Nesprin and SUN components of LINC complex were depleted^[36–38] or when the nucleus was softened by depleting LaminA/C.^[39] To this point, we previously reported that depleting LINC function does not soften cell nuclei;^[40] the preservation of nuclear modulus suggests that interfering with actin/Nesprin attachment stimulates compensatory processes to losing nucleocytoplasmic connectivity by upregulating attachments at the cell edge.

As to effects in MSC, it has been recently reported that depleting LINC function via depletion of SUN proteins can alter heterochromatin states altering lineage selection.^[41] Depleting

SUN proteins results in functionally different heterochromatin rearrangements than does dnKASH expression,^[21] suggesting that changes in the heterochromatin state are affected by both nuclear envelope structural composition and F-actin contractility. To this end, our method can be implemented with both fixed and live cell imaging to detect changes in F-actin under variety of mechanical forces and thus enable researchers to develop new hypotheses in cell mechanobiology.

Supporting Information

Supporting Information is available from the Wiley Online Library or from the author.

Acknowledgements

This study was supported by AG059923, AR075803, P20GM109095, NSF1929188, and NSF 2025505.

Conflict of Interest

The authors declare no conflict of interest.

Author Contributions

N.N.: Concept/design, data analysis/interpretation, manuscript writing; N.B.: data analysis/interpretation, manuscript writing; M.G.: data analysis/interpretation, manuscript writing; M.G.: interpretation, manuscript writing; C.C.: data analysis, final approval of manuscript; S.H.: data analysis, final approval of manuscript; A.Z.: data analysis, final approval of manuscript; J.R.: concept/design, data analysis/interpretation, final approval of manuscript; A.S.: concept/design, data analysis/interpretation, financial support, manuscript writing, final approval of manuscript; G.U.: concept/design, data analysis/interpretation, financial support, manuscript writing, final approval of manuscript.

Data Availability Statement

The data that support the findings of this study are available in the supplementary material of this article.

Keywords

cytoskeleton, F-actin, linker of nucleoskeleton and cytoskeleton, machine learning, mechanobiology, nuclear envelope

Received: June 12, 2023

Revised: January 7, 2024

Published online: February 16, 2024

- [1] S. B. Khatau, D. H. Kim, C. M. Hale, R. J. Bloom, D. Wirtz, *Nucleus* **2010**, *1*, 337.
- [2] B. Özdemir, R. Reski, *Comput. Struct. Biotechnol. J.* **2021**, *19*, 2106.
- [3] A. B. Schroeder, E. T. A. Dobson, C. T. Rueden, P. Tomancak, F. Jug, K. W. Eliceiri, *Protein Sci.* **2021**, *30*, 234.
- [4] J.-K. Kim, A. Louhghalam, G. Lee, B. W. Schafer, D. Wirtz, D.-H. Kim, *Nat. Commun.* **2017**, *8*, 2123.

- [5] J. G. McGarry, J. Klein-Nulend, M. G. Mullender, P. J. Prendergast, *FASEB J.* **2005**, *19*, 482.
- [6] M. Saeed, D. Weihs, *Biomech. Model. Mechanobiol.* **2019**, *18*, 717.
- [7] P. Kanchanawong, G. Shtengel, A. M. Pasapera, E. B. Ramko, M. W. Davidson, H. F. Hess, C. M. Waterman, *Nature* **2010**, *468*, 580.
- [8] Y. Liu, K. Mollaeian, J. Ren, *Electronics* **2018**, *7*, 443.
- [9] B. Eltzner, C. Wollnik, C. Gottschlich, S. Huckemann, F. Rehfeldt, *PLoS One* **2015**, *10*, e0126346.
- [10] M. Alioscha-Perez, C. Benadiba, K. Goossens, S. Kasas, G. Dietler, R. Willaert, H. Sahli, *PLoS Comput. Biol.* **2016**, *12*, e1005063.
- [11] T. Xu, D. Vavylonis, F.-C. Tsai, G. H. Koenderink, W. Nie, E. Yusuf, J.-Q. Wu, X. Huang, *Sci. Rep.* **2015**, *5*, 9081.
- [12] N. S. Rossen, A. Kyrsting, A. J. Giaccia, J. T. Erler, L. B. Oddershede, *Biophys. J.* **2021**, *120*, 3860.
- [13] S. G. Alam, Q. Zhang, N. Prasad, Y. Li, S. Chamala, R. Kuchibhotla, B. KC, V. Aggarwal, S. Shrestha, A. L. Jones, S. E. Levy, K. J. Roux, J. A. Nickerson, T. P. Lele, *Sci. Rep.* **2016**, *6*, 38063.
- [14] G. Uzer, W. R. Thompson, B. Sen, Z. Xie, S. S. Yen, S. Miller, G. Bas, M. Styner, C. T. Rubin, S. Judex, K. Burridge, J. Rubin, *Stem Cells* **2015**, *33*, 2063.
- [15] S. Ghosh, B. Seelbinder, J. T. Henderson, R. D. Watts, A. K. Scott, A. I. Veress, C. P. Neu, *Cell Rep.* **2019**, *27*, 1607.
- [16] M. Spichal, A. Brion, S. Herbert, A. Cournac, M. Marbouty, C. Zimmer, R. Koszul, E. Fabre, *J. Cell Sci.* **2016**, *129*, 681.
- [17] J. Link, D. Jahn, M. Alsheimer, *Nucleus* **2015**, *6*, 93.
- [18] F. Lottersberger, R. A. Karssemeijer, N. Dimitrova, T. de Lange, *Cell* **2015**, *163*, 880.
- [19] R. K. Swartz, E. C. Rodriguez, M. C. King, *Mol. Biol. Cell* **2014**, *25*, 2461.
- [20] A. Peister, J. A. Mellad, B. L. Larson, B. M. Hall, L. F. Gibson, D. J. Prockop, *Blood* **2004**, *103*, 1662.
- [21] M. Goelzer, S. Howard, A. Zavala, D. Conway, J. Rubin, A. J. van Wijnen, G. Uzer, (Preprint) bioRxiv, submitted: Apr. **2022**.
- [22] G. Dennis, B. T. Sherman, D. A. Hosack, J. Yang, W. Gao, H. C. Lane, R. A. Lempicki, *Genome Biol.* **2003**, *4*, R60.
- [23] C. McQuin, A. Goodman, V. Chernyshev, L. Kamentsky, B. A. Cimini, K. W. Karhohs, M. Doan, L. Ding, S. M. Rafelski, D. Thirstrup, W. Wiegraebe, S. Singh, T. Becker, J. C. Caicedo, A. E. Carpenter, *PLoS Biol.* **2018**, *16*, e2005970.
- [24] K. Nagayama, Y. Yahiro, T. Matsumoto, *Cell. Mol. Bioeng.* **2013**, *6*, 473.
- [25] T. Falk, D. Mai, R. Bensch, Ö. Çiçek, A. Abdulkadir, Y. Marrakchi, A. Böhm, J. Deubner, Z. Jäckel, K. Seiwald, A. Dovzhenko, O. Tietz, C. D. Bosco, S. Walsh, D. Saltukoglu, T. L. Tay, M. Prinz, K. Palme, M. Simons, I. Diester, T. Brox, O. Ronneberger, *Nat. Methods* **2019**, *16*, 67.
- [26] O. Ronneberger, P. Fischer, T. Brox, in *Medical Image Computing and Computer-Assisted Intervention – MICCAI 2015* (Eds: N. Navab, J. Hornegger, W. M. Wells, A. F. Frangi), Springer International Publishing, Cham **2015**, pp. 234–241.
- [27] A. K. Singh, H. H. Lin, *Biomed. J.* **2021**, *44*, 534.
- [28] S. Barbera, L. Raucci, R. Lugano, G. M. Tosi, A. Dimberg, A. Santucci, F. Galvagni, M. Orlandini, *Int. J. Mol. Sci.* **2021**, *22*, 12417.
- [29] M. Versaavel, J.-B. Braquénier, M. Riaz, T. Grevesse, J. Lantoiné, S. Gabriele, *Sci. Rep.* **2014**, *4*, 7362.
- [30] K. Abhishek, G. V. Shivashankar, *Methods Appl. Fluoresc.* **2016**, *4*, 044008.
- [31] D. B. Lovett, N. Shekhar, J. A. Nickerson, K. J. Roux, T. P. Lele, *Cell. Mol. Bioeng.* **2013**, *6*, 230.
- [32] G. Uzer, S. Pongkitwitoon, C. Ian, W. R. Thompson, J. Rubin, M. E. Chan, S. Judex, *PLoS One* **2014**, *9*, e90840.

- [33] G. Tang, M. Galluzzi, B. Zhang, Y. L. Shen, F. J. Stadler, *Langmuir* **2019**, *35*, 7578.
- [34] J. S. Milner, M. W. Grol, K. L. Beaucage, S. J. Dixon, D. W. Holdsworth, *J. Funct. Biomater.* **2012**, *3*, 209.
- [35] J. D. Salvi, J. Y. Lim, H. J. Donahue, *Tissue Eng., Part C* **2009**, *16*, 661.
- [36] A. Woychek, J. C. R. Jones, *Cytoskeleton* **2019**, *76*, C1.
- [37] T. J. Chancellor, J. Lee, C. K. Thodeti, T. Lele, *Biophys. J.* **2010**, *99*, 115.
- [38] L. Porter, R.-M. Minaisah, S. Ahmed, S. Ali, R. Norton, Q. Zhang, E. Ferraro, C. Molenaar, M. Holt, S. Cox, S. Fountain, C. Shanahan, D. Warren, *Cells* **2020**, *9*, 132.
- [39] M. Goelzer, A. Dudakovic, M. Olcum, B. Sen, E. Ozcivici, J. Rubin, A. J. van Wijnen, G. Uzer, *Int. J. Mol. Sci.* **2021**, *22*, 6580.
- [40] J. Newberg, J. Schimpf, K. Woods, S. Loiate, P. H. Davis, G. Uzer, *J. Biomech.* **2020**, *111*, 110012.
- [41] D. A. Pavlov, C. P. Unnikannan, D. Lorber, G. Bajpai, T. Olender, E. Stoops, A. Reuveny, S. Safran, T. Volk, *Cells* **2023**, *12*, 932.